Journal of Materials Chemistry A

Influence of hydrogen and oxygen on the structure and properties of sputtered magnesium zirconium oxynitride thin films

Journal:	*Journal of Materials Chemistry A*
Manuscript ID	TA-ART-01-2020-000654.R2
Article Type:	Paper
Date Submitted by the Author:	16-Apr-2020

Complete List of Authors:	Kim, Jekyung; Korea Advanced Institute of Science and Technology, Department of Materials Science and Engineering Bauers, Sage; National Renewable Energy Laboratory, Materials Science Center Khan, Imran; National Renewable Energy Laboratory, Materials Science Center Perkins, John; National Renewable Energy Laboratory, Park, Bo-In; Korea Advanced Institute of Science and Technology, Department of Materials Science and Engineering Talley, Kevin; National Renewable Energy Laboratory, Materials Science Center; Colorado School of Mines, Department of Metallurgical and Materials Engineering Kim, Daehan; Korea Advanced Institute of Science and Technology, Department of Materials Science and Engineering Zakutayev, Andriy; National Renewable Energy Laboratory, Materials Science Center Shin, Byungha; Korea Advanced Institute of Science and Technology, Department of Materials Science and Engineering

Influence of hydrogen and oxygen on the structure and properties of sputtered magnesium zirconium oxynitride thin films

Jekyung Kim[1,2], Sage R. Bauers[1], Imran S. Khan[1], John Perkins[1], Boin Park[2], Kevin R. Tally[1,3], Daehan Kim[2], Andriy Zakutayev[*1], and Byungha Shin[*2]

[1] Materials Science Center, National Renewable Energy Laboratory, Golden, Colorado, 80401, United States

[2] Department of Materials Science and Engineering, Korea Advanced Institute of Science and Technology, Daejeon, 34141, South Korea

[3] Department of Metallurgical and Materials Engineering, Colorado School of Mines, Golden, Colorado, 80401, United States

*corresponding authors

Abstract

Nitride materials with mixed ionic and covalent bonding character and resulting good charge transport properties are attractive for optoelectronic devices. Recently, Mg-based ternary nitride materials were found to have large dielectric constants and high absorption coefficients with bandgaps appropriate for photovoltaic applications. However, their degenerate carrier concentrations still hinder from possible applications into solar cells or related optoelectronic devices. Therefore, further understanding and engineering of the parameters controlling materials properties of these ternary nitrides is highly desirable. Here we report that structural, optical and electrical properties of magnesium zirconium oxynitride (MZNO) thin films synthesized by combinatorial sputtering with a wide range of cation compositions can be affected by incorporation of oxygen and hydrogen. Excess oxygen improved crystallinity of MZNO thin films whereas

hydrogen attracted oxygen and formed Mg-rich oxide layers at grain boundaries which in turn reduced the conductivity. On the other hand, optical properties are more sensitive to the composition–both cation and anion ratio–rather than the presence of hydrogen. Compared to cation-stoichiometric MZNO (10^{19} – 10^{20} cm^{-3}), substantial reduction of carrier concentration down to ~10^{14} cm^{-3} was achieved at Mg-rich conditions by supplying hydrogen during growth. Photoluminescence measurements showed that films prepared with hydrogen were optoelectronically active. Overall, this study demonstrates that material properties of MZN thin films can be significantly influenced by incorporation of oxygen and hydrogen.

Introduction

Binary nitride thin films are widely used in several technological applications such as light emitting diodes (LED) and other optoelectronics, micromechanical actuators used for telecommunications, protective coating layers and diffusion barriers in semiconducting industry, and others.[1-8]This diverse suite of applications result from the wide range of properties in nitrides: e.g. 3.4 eV for GaN, 6.2 eV for AlN, 1.0 eV for Cu_3N, or 1.5 eV for Sn_3N_4.[9-15] Nitrides exhibit higher defect tolerance than other pnictides because higher electronegativity of nitrogen renders nitrides more ionic, thereby forming shallower defect states.[16, 17] Meanwhile, nitrides are more covalent than oxides, which results in lower bandgaps and enhanced charge transport. Taken together, the established technological suitability, range of bandgaps, and favorable bonding properties of nitrides present a compelling platform for applications towards photovoltaic (PV) devices.

Recently, cation-mutated ternary nitrides, where the group III^{3+} element of a binary nitride is replaced with group II^{2+} and group IV^{4+} elements (III^{3+}-N $\rightarrow$ II^{2+}-IV^{4+}-N_2), have drawn significant attention. These heterovalent analogues to binary nitrides can exhibit tunable electronic and optical properties suitable for PV and LEDs as well as high defect-tolerance.[18-21] For example, $ZnSnN_2$ exhibits desirable properties as a PV absorber with a high absorption coefficient, a direct bandgap of 1.4 eV, and carrier concentrations below 10^{17} cm^{-3}.[19, 21] Another emerging class of such ternary nitrides is Mg-TM-N_2, where TM represents a group-4 transition metal. When an alkaline earth metal such as Mg^{2+} is alloyed with a transition metal nitride, electropositive Mg^{2+} drives the transition metal into a higher oxidation state, yielding semiconducting behavior by forming Mg-TM-N_2.[22-24] Experimental demonstrations of semiconducting properties of $MgTiN_2$, $MgHfN_2$, and $MgZrN_2$ have also been reported recently, confirming the computational predictions.[25-29]

These Mg-based ternary nitrides exhibit a high absorption coefficient with an optical absorption onset around 1.7 eV, in an ideal range for PV applications. Mg-TM-N_2 also possess a relatively large static dielectric constant (25 - 75 ε_0), making them an even more suitable for electronic applications due to better screening of carriers from charged defects.[30-34] However, the primary challenge in using the Mg-based nitrides as a photo absorber is their computationally predicted indirect character of their bandgaps and degenerate carrier densities on the order of $>10^{18}$ cm^{-3}.[26, 27] Therefore, better understanding and control of these materials is necessary to take advantage of the otherwise excellent properties for PV and electronic applications.

Herein we report on changing structural, optical, and electrical properties of ternary $Mg_xZr_{1-x}N_y$ (MZN) thin films with different cation compositions by incorporation of oxygen and hydrogen. MZN thin films exhibited electron concentration of $\sim10^{17}$ - 10^{18} cm^{-3} or $\sim10^{19}$ - 10^{20} cm^{-3} depending on Mg and O content. Surprisingly, 10x reduction of the carrier density was achieved by incorporation of oxygen in Mg-rich samples, with absorption spectra showing more semiconducting behavior. Further reduction of carrier concentration was demonstrated by supplying hydrogen during the sputter growth, with measured carrier concentrations on the order of 10^{14} cm^{-3}. Moreover, photoluminescence spectra indicate this material became opto-electronically active with the incorporation of oxygen and hydrogen. These results represent an important step towards the potential use of MZN in PV and other optoelectronic devices.

Methods

1. Synthesis

MZN thin films were fabricated using a high-throughput experimental (combinatorial) technique. Two sputter guns were positioned 180° opposed to each other but obliquely aligned to

the substrate plane, so that a one-dimensional composition gradient naturally formed within each thin film—Mg-rich on one end and close to stoichiometric $MgZrN_2$ on the other end. We refer to each film as a "library" consisting of 44 samples: 4 at each one of 11 compositions. The MZN thin films were deposited on corning Eagle XG glass (structure and properties) and glassy C (composition).

Oxygen-rich MZN thin films were deposited by RF sputtering using Mg (2 in. diameter, 99.98%, Kurt J. Lesker) and Zr (2 in. diameter, Grade 702, Kurt J. Lesker) targets at a working pressure of 10 mTorr. A mixture of N_2 and Ar gas was introduced during deposition each at a flow rate of 8 sccm, as determined by mass flow controllers. Prior to the deposition, the sputtering system was evacuated using a cryogenic pump to a base pressure of 6.0 – 7.0 x 10^{-7} torr. The passive partial pressures of H_2O and OH, which are the main sources of oxygen in the as-deposited films, were on the order of 10^{-7} torr while that of O_2 were below 10^{-8} torr, according to residual gas analyzer (RGA) installed on a chamber. Attempts to intentionally flow oxygen into the growth chamber resulted in pure oxide rather than oxynitride films. The substrate temperature was set to 400 °C (measured with a thermocouple) with a thermal contact of Ag paint behind the substrate. To incorporate hydrogen MZN thin films were grown with the same oxygen-rich conditions, but with pure N_2 replaced by a forming gas (5 %H_2/95 %N_2) with a flow rate 8 sccm..

Oxygen-free MZN thin films were fabricated in a similar but separate sputtering system, installed with a cryogenic shroud, a sample load-lock, and a nitrogen plasma source, as described in previous literature.[26, 27] The chamber was baked for 3 days to reduce the partial pressures of oxygen-containing species (H_2O, OH, O_2) below 10^{-8} torr prior to growth. Oxygen-free MZN thin films were deposited at a pressure of 5 mTorr under 6 sccm flows of both N_2 and Ar, from Mg and Zr targets on substrates heated to 400 °C.

2. Characterization

The structural properties of MZN thin films were studied using an X-ray diffractometer (XRD; Bruker D8) equipped with a 2D detector. The composition of libraries was analyzed using Rutherford backscattering (RBS; National Electrostatics Corp) measurement. Optical measurements were performed using ultraviolet-visible spectroscopy (UV-Vis; Ocean Optics), and electrical sheet resistances were measured using a customized 4 point-probe system (4PP). Each of these spatially-resolved characterizations (XRD, RBS, UV-Vis, and 4PP) were carried out either for all 44 samples of a library or for 11 samples along one of the 4 redundant rows. With the except of 4PP, each probe's spot size was $\leq$ 1mm diameter.

For selected samples, high-resolution structural and chemical analysis were performed by scanning transmission electron microscopy (STEM; FEI Talos F200X) equipped with Super-X energy dispersive X-ray spectroscopy (EDS) detector. The specimens for STEM analysis were prepared using a dual beam focused ion beam (FIB, FEI Nova 600 NanoLab) with an accelerating voltage of 5 - 30 kV. Secondary-ion mass spectrometry (SIMS; ION-TOF GmbH) depth profile was obtained using TOF-SIMS. An area of 100 x 100 μm^2 was analyzed with primary ions of Bi^+ with 30 keV ion energy to detect sputter-etched ions from the surface. Cs^+ with 2 keV energy and 600 nA ion current was used to sputter the sample in an area of 300 x 300 μm^2. Electronic properties of a subset of MZN samples were also characterized by a Hall effect measurement (Lake Shore Cryotronics Model 8425) from 100 K to 300 K. Low temperature photoluminescence (PL; Horiba LabRAM HR Evolution) measurements were performed using a 514 nm excitation laser.

Results and Discussion

1. Composition and Structure

The compositions of magnesium zirconium oxynitride (MZNO) were measured by RBS, and are shown in Fig. 1. For oxygen-rich MZNO, oxygen anion ratio (i.e. Y = O/(N+O)) increased from 0.12 to 0.25 in a single library with increasing magnesium cation ratio (i.e. X = Mg/(Mg+Zr)) with an empirical fitting line of Y = 0.5(X - 0.5) + 0.12. For zinc tin oxynitride (ZTNO), a [Zn_{Sn} + $2O_N$] defect compensation mechanism has been proposed to rationalize similar behavior but with dY/dX = 2.0.[35, 36] The differences in slope suggest the defect compensation mechanism in MZNO is different from ZTNO. Regardless of whether films were grown in pure N_2 or H_2/N_2, MZNO films showed similar oxygen concentrations when partial pressures of O_2 and H_2O were similar. This is consistent with previous experimental observations in ZTNO, where oxygen concentration was controlled by the oxygen level of the residual gases (O_2 and H_2O) during growth.[21, 35]

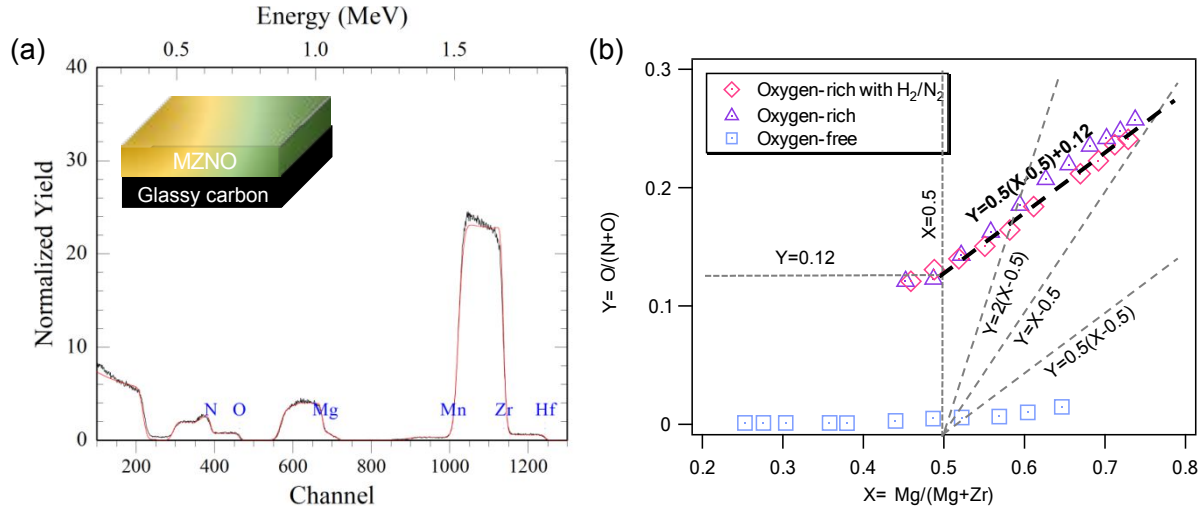

Fig. 1 (a) RBS spectrum of $Mg_{1.31}Zr_{0.69}N_{1.84}O_{0.52}$ film on glassy carbon substrate (Inset shows a cross-sectional schematic drawing), and (b) anion and cation composition gradients of MZNO libraries

The structural properties of MZNO are affected by both cation and anion-ratio. As shown

in Fig. 2, MZNO thin films exhibit a rocksalt-derived structure without any evidence for secondary phases such as ZrN or MgO (see Fig. S1). The rocksalt-derived structure is maintained even up to 25 % O/(N+O) (Fig. S2). However, when the amount of oxygen further increases, the MZNO thin films become transparent and phase-segregate into MgO and ZrO_2 (data not shown). In Mg-rich samples the (111) peak intensity increases relative to (200), similar to oxygen-free MZN (see Fig. S2).[26, 27] For a given oxygen level only a very small peak-shift to a smaller 2θ with increasing Zr is observed since octahedral Mg^{2+} and Zr^{4+} ionic radii are similar.[37]

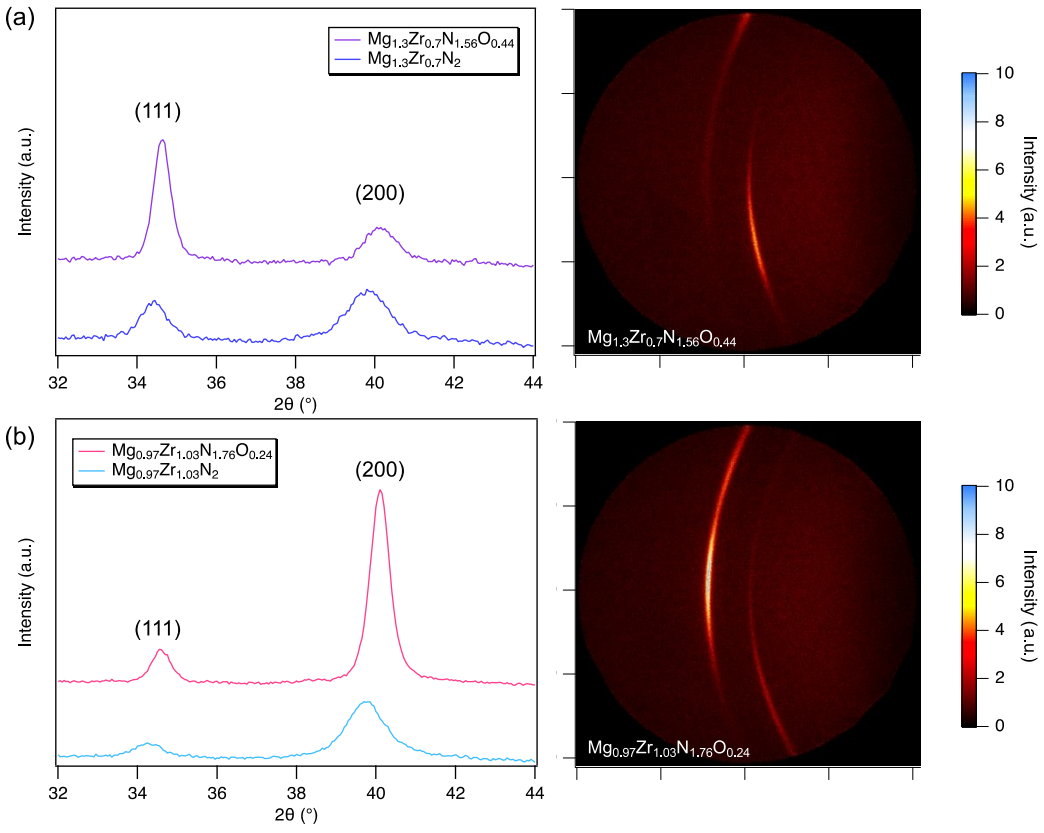

Fig. 2 X-ray diffraction (XRD) pattern for (a) Mg-rich and (b) Zr-rich MZNO thin films for different amounts of oxygen. The right column of each panel shows the 2D detector image of MZNO thin films demonstrating the preferential orientations depending on Mg/(Mg+Zr).

It is interesting to note that introduction of oxygen leads to narrower full-width-half-maximum and higher intensity, as shown in Fig. 2a and 2b. However, this difference may be also attributed to differences in other deposition parameters between MZNO and MZN, such as target-to-substrate distance and angle, total pressure, and etc. Similar peak widths/intensities are observed when supplying hydrogen during growth (Fig. S3), suggesting that hydrogen does not influence the crystallinity of MZN. With increasing oxygen, peaks shift to larger 2θ's, similar to other oxynitrides such as $Zn_xO_yN_x$[38] or $TiO_{1-x}N_x$[39]. The lattice parameters calculated from XRD are in reasonable agreement with TEM (Fig. S4).

Microstructure of MZNO was investigated by TEM analysis. High angle annular dark-field scanning TEM (HAADF-STEM) micrographs and EDS elemental maps are shown in Fig. 3. All films exhibit a columnar structure commonly seen in sputter-grown thin films. A grain size of ~20 nm is observed for MZN and MZNO regardless of oxygen and hydrogen presence during deposition, and the top surface is oxidized irrespective of the growth condition. Nitrogen is uniformly distributed throughout the bulk of MZN, and for MZNO an even distribution of both nitrogen and oxygen is observed except for small oxygen excess in grain boundaries. The cations are distributed such that grain boundaries are slightly Mg-rich and Zr-poor. Interestingly, when hydrogen was incorporated, oxygen and magnesium were strongly segregated at grain boundaries, forming a Mg-rich oxide layer as confirmed by line-scan shown in Fig. S4. One may consider the oxygen-rich grain boundaries as a 'second phase', but it is not a separate two-phase structure of MgO and ZrN phase considering that relatively homogenous distributions of Mg-Zr-N-O was observed in the bulk except for grain boundaries in Fig. S4(c). Moreover, in Fig. S1 and Fig 2b, XRD peaks for oxygen-rich samples (i.e. MZNO) are actually narrower compared to oxygen-free

samples (i.e. MZN), further indicating that the presence of two-phases is rather unlikely.

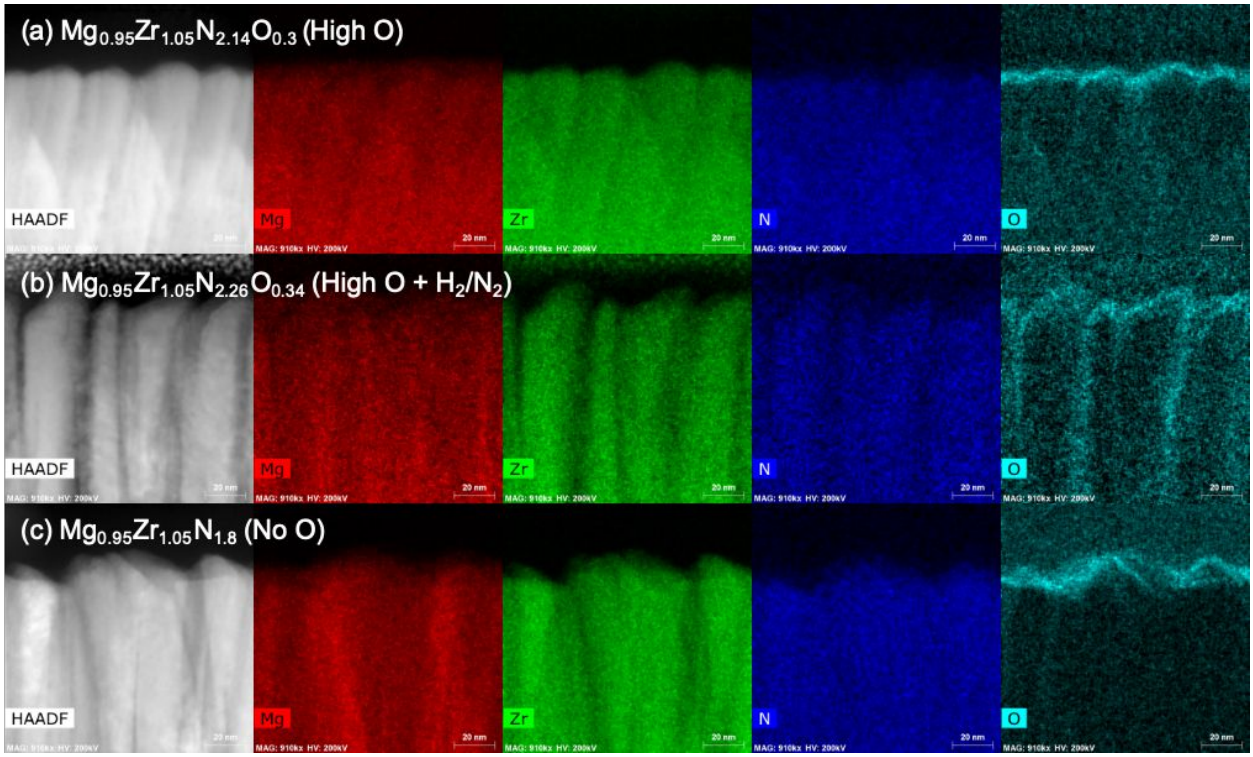

Fig. 3 HAADF-STEM images and corresponding EDS mapping for MZNO thin films, including (a) $Mg_{0.95}Zr_{1.05}N_{2.14}O_{0.3}$, (b) $Mg_{0.95}Zr_{1.05}N_{2.26}O_{0.34}$ deposited with H_2/N_2, and (c) $Mg_{0.95}Zr_{1.05}N_{1.8}$ without O_2 or H_2

When MZNO (grown both with and without hydrogen) was post-annealed in air (for 5 minutes at 300 ^oC), we also found oxygen segregation at grain boundaries. This is similar to observations in Fig. 3b and S4. Therefore, we conclude that when hydrogen is incorporated during growth, it attracts oxygen and re-distributes it to grain boundaries.

Table 1. Thermodynamic properties for Mg-O, Mg-N, Zr-O, Zr-N phases, including

experimental Gibbs Free energies ΔG^{o}_{exp} at 298K and 1atm,[40, 41] and theoretical Formation Enthalpies ΔH^{o}_{theor} (from https://materials.nrel.gov/)[42]

Material	ΔG^{o}_{exp} **(kJ/mol)**	ΔH^{o}_{theor} **(eV/f.u.)**
ZrO_2	-1042.7 ± 1.3	-11.49
ZrN	-341.8 ± 2.0	-3.82
Zr_3N_4	unknown	-12.18
MgO	-569.4	-6.26
Mg_3N_2	-406.0	-5.25
$MgZrN_2$	unknown	-6.48

At a first glance, the presence of Mg-rich oxide in grain boundaries observed by TEM/EDS (Fig. 3) is unexpected. The experimentally measured formation energy for MgO (-569.4 KJ/mol) is less negative than that of ZrO_2 (-1042.7 KJ/mol) as seen from Table 1, therefore ZrO_2 is expected to form easier than MgO. However, the relevant balanced reactions that describe the oxidation process are:

$$2Mg_3N_2 + 3O_2 \rightarrow 6MgO + 2N_2 \quad (1)$$

and

$$2ZrN + 2O_2 \rightarrow 2ZrO_2 + N_2 \quad (2a)$$

or

$$Zr_3N_4 + 3O_2 \rightarrow 3ZrO_2 + 2N_2 \quad (2b)$$

The enthalpy of reaction-1 (ΔH_{theor} = -27.1 eV, ΔG^{o}_{exp} = -2602 KJ) is larger than for reaction-2a (ΔH_{theor} = -15.3 eV, ΔG^{o}_{exp} = -1402 KJ) or reaction-2b (ΔH_{theor} = -22.3 eV), which explains why Mg rather than Zr is preferentially oxidized in MZNO grain boundaries. These differences are even larger when formation enthalpies of molecular oxygen (-9.4 eV) and nitrogen (-15.4 eV) are taken into account, since a fraction of them may be atomized during the sputtering process. The calculated formation enthalpy of $MgZrN_2$ is also presented in Table 1.

2. Electronic and Optical Properties

Optical properties of MZNO thin films were measured using UV-Vis spectroscopy and absorbance spectra are shown in Fig. 4. The optical absorption edge increases at low Mg/(Mg+Zr) due to free carrier absorption. However, a sharp absorption onset was observed for MZNO with high Mg/(Mg+Zr) because free carriers are compensated with increasing Mg. This compositional dependence (in terms of cation ratio) has already been observed with oxygen-free MZN.[27] These results are also consistent with what has been observed in $Zn_{1+x}Sn_{1-x}N_2$ in that ZTN with a low Zn/(Zn+Sn) ratio (< ~0.6) exhibited a high absorption at low energy due to its high carrier density of around 10^{20} cm^{-3}.[19] Additional absorption spectra in correlation with a cation ratio in a single library of MZNO are presented in Fig. S5. In Fig. S5, with decreasing Mg/(Mg+Zr) (i.e. increasing carrier density), only the absorption (in y-axis) increases at lower energies due to free carrier absorption while the energy shift (in x-aixs) is not present at higher energy. Therefore, there is no dependence of optical bandgap on the carrier density. Also, the electron effective mass of this material is 0.6-1.3,[26] which is x2-4 heavier than that of ITO[43-45] where a Burnstein-Moss (B-M) shift is known to occur above at a carrier concentration of 10^{20} cm^{-3}.[46] Since the effective masses of MZN are heavier, the B-M shift is unlikely to occur at 10^{20} cm^{-3} and below.

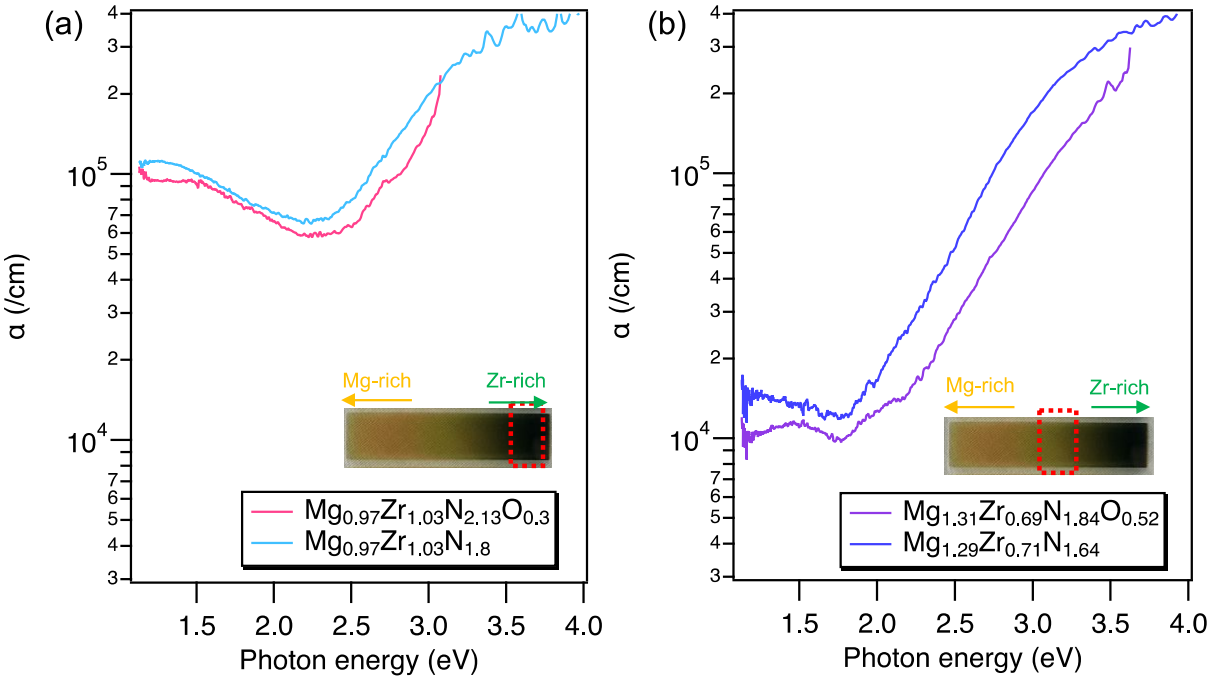

Fig. 4 UV-Vis absorption spectra for (a) Zr-rich and (b) Mg-rich MZNO thin films depending on the amount of oxygen. Insets in each panel show a photograph of the MZNO library. The measured area was marked with a dashed square.

With increasing oxygen concentration, the overall absorptivity decreases and the absorption onset observed at high Mg/(Mg+Zr) shifts to a higher energy (Fig. 4b). First-principles calculations combined with Monte-Carlo simulations were recently conducted for semiconducting ZTN with the consideration of non-ideality factors such as off-stoichiometry, disorder, and incorporation of oxygen.[35] This study modeled the composition-dependent band edge position and found that the ZTN conduction band minimum shifts upward at oxygen- and Zn-rich conditions, leading to an apparent widening of the bandgap.[35] A similar shift may be expected in the case of MZNO when compared to pure MZN, but with a different underlying microscopic mechanism of

defect compensation as suggested by the interdependence between anion and cation ratio of MZNO (Fig. 1b). On the other hand, when hydrogen was introduced during MZNO growth, samples showed negligible difference of the absorption spectra as shown in Fig. S5. Therefore, both the cation and anion ratios of MZN play a more critical role in determining the optical properties than the presence of hydrogen during the growth.

The electrical conductivity of MZNO at various compositions is shown in Fig. 5a. Regardless of the existence of oxygen, the films exhibited more insulating behavior with increasing Mg, changing over 3 orders of magnitude from ~ 1 S/cm for Mg/(Mg+Zr) ~0.485 to ~10^{-3} S/cm for Mg/(Mg+Zr) ~0.65. MZNO with Mg/(Mg+Zr) > 0.65 showed resistances above the detection limit of the four-point probe system. To further study the electronic properties of MZNO, temperature-dependent Hall effect measurements were performed (Fig. S6) showing weakly temperature-activated transport for all samples.

Fig. 5b presents room-temperature carrier concentrations collected from samples with nearly-stoichiometric (Mg/(Mg+Zr) = 0.485) and Mg-rich (Mg/(Mg+Zr) = 0.65) cation compositions and varying oxygen concentrations. Immediately clear is that oxygen increases the carrier density in cation-stoichiometric samples and decreases the carrier density in Mg-rich samples. This difference is possibly due to the different ways oxygen creates vs compensates defects. For stoichiometric cation compositions, O_N likely acts as an electron-donating defect. On the other hand, we speculate that at high Mg fractions $Mg_{Zr} + O_N$ defect complexes might provide a mechanism for compensating cation off-stoichiometry. This is in agreement with computational theory of doping and defect properties of $ZnSnN_2$.[35] It was found that at a low doping level of oxygen, the single donor O_N^{1+} increases carrier concentration. At higher concentrations oxygen couples with excess Zn to passivate O_N donor defects. The Mg_{Zr} in this

paper is meant to represent excess Mg on the cation sub-lattice, rather than point to substitution of Mg or a specific Zr site. This defect notation is conventional in literature on other cation-disordered II-IV-N_2 materials.[35, 36]

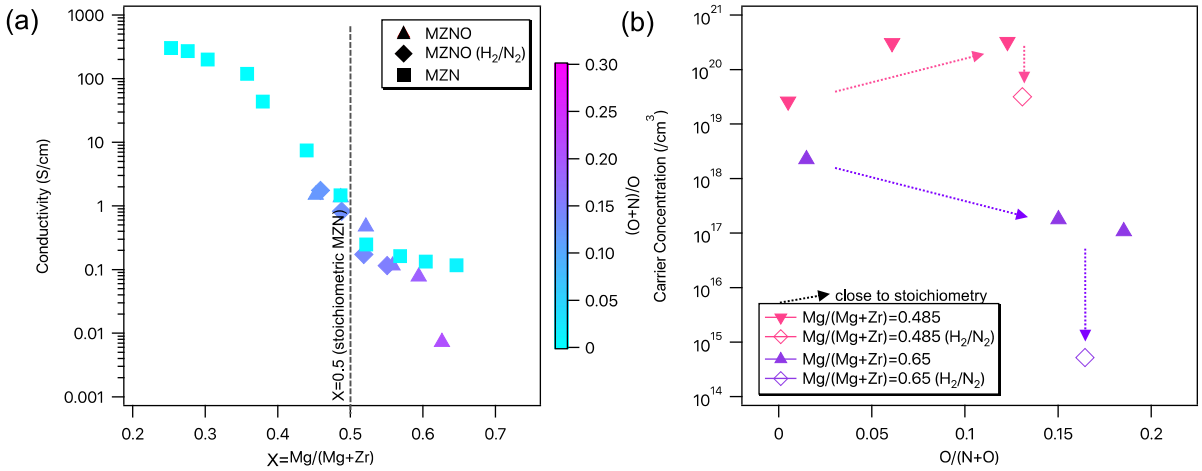

Fig. 5 Change in (a) conductivity, and (b) electron concentration MZNO thin films depending on the composition and incorporation of hydrogen

Significant reduction of the electron concentration in MZNO was realized by supplying hydrogen during growth of the Mg-rich material, resulting in a carrier density decrease from 10^{17} cm^{-3} to < 10^{15} cm^{-3}. On the other hand, for stoichiometric cation composition a smaller effect was observed. Whereas the n-type carrier density increased from 10^{19} cm^{-3} to 10^{20} cm^{-3} up to 12.5% oxygen anion fraction, it decreased back to the oxygen-free level of 10^{19} cm^{-3} when hydrogen was introduced during growth. Overall, these experimental observations lead to the conclusion that controlling donor defects such as O_N either by excess of O or presence of hydrogen, both coupled to cation composition, is important for tuning carrier concentration of MZN.

In $ZnSnN_2$, it has been reported that incorporating hydrogen during growth can reduce the

carrier density by an order of magnitude, and that further annealing under N_2 dramatically decreases the carrier concentration down to $<10^{17}$ cm^{-3}.[21] The mechanism was attributed to hydrogen passivation of acceptors (Zn_{Sn}) by forming neutral Zn-H complexes and preventing the formation of compensating donor defects. Under further annealing, dissociation of Zn-H activates Zn_{Sn} acceptors to reduce the n-type carrier concentration.[21] Similar mechanisms might be expected in MZNO, where hydrogen may form and dissociates Mg-H complexes[47, 48] preventing the formation of additional donor defects. The incorporation of hydrogen in MZNO was revealed by SIMS depth profile in Fig. S7. The hydrogen content of the MZNO grown under H_2/N_2 is x2-3 higher than the MZNO grown under pure N_2. Considering that the partial pressure (measured by RGA) of hydrogen-containing species such as H_2O before deposition was similar in both cases, the increased hydrogen content was from the flow of H_2/N_2. The larger hydrogen concentration must have led to the formation of Mg-H complexes, which reduced the carrier concentration.

Moreover, controlling donor defects somewhat influences the mobility as seen from Fig. S8. Overall, the mobility is on the order of 0.1 – 0.5 cm^2/Vs, due to polycrystalline microstructure; higher mobility in the 10-100 cm^2/Vs range can be achieved in epitaxial films.[26, 49] For the stoichiometric cation composition, mobility decreased with increasing oxygen, likely due to the formation of donor-like O_N which results in a higher level of ionized scattering. For the Mg-rich samples, however, the likely compensation of donor defects by partial formation of Mg_{Zr} and formation of defect complexes would reduce carrier density, hence less scattering. Interestingly, when hydrogen is incorporated, the mobility increased by x2-3 higher regardless of oxygen. One might also expect the decrease in the mobility due to the presence of oxide layers at grain boundaries as evidenced by Fig. 3. However, passivation of donor defects in the presence of hydrogen resulted in the less ionized defect scattering. Similarly, in the previous reports on the

mobility of $ZnSnN_2$,[36] the mobility changed more significantly with the carrier density due to composition and annealing, while the microstructure remained the same. Therefore, we conclude the mobility is governed more significantly by the ionized defect scattering than grain boundaries.

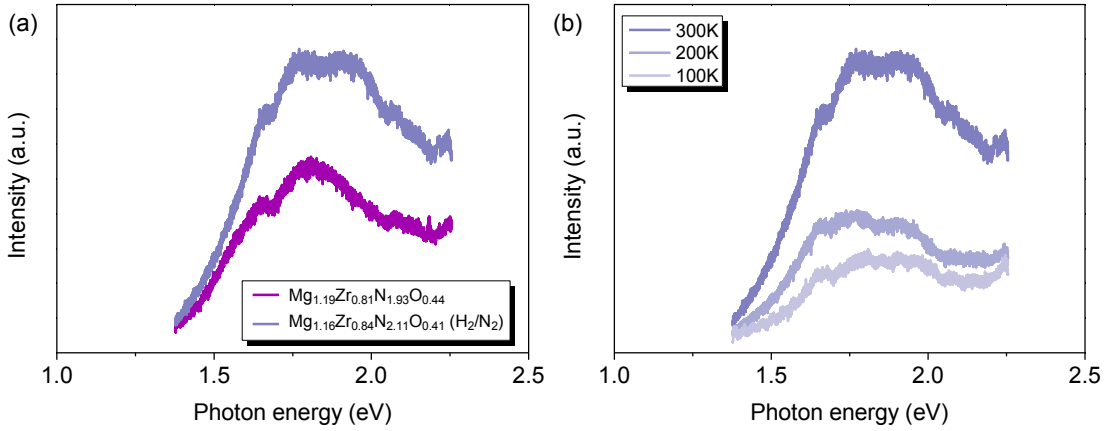

Fig. 6 Photoluminescence spectra for (a) MZNO thin films at 300K depending on the incorporation of hydrogen, and temperature-dependent PL spectra for (b) MZNO thin films grown under H_2/N_2 (Mg/(Mg+Zr) = 0.6).

To further understand defect chemistry of MZNO, we performed temperature-dependent photoluminescence (PL) measurements. Pure MZN exhibited no measurable PL signal (data not shown) while MZNO emitted a broad PL peak centered around 1.7-1.8 eV (Fig. 6a). Hydrogen further contributes to the increase in PL intensity, suggesting that the activation of acceptors (or passivation of donors) should enhance the radiative recombination. For MZNO with hydrogen, a PL peak at a higher energy (~1.9 eV) emerged, apparently broadening the overall width of the PL spectrum. We speculate that this is related to either acceptor-like defects such as Mg_{Zr} or neutral Mg-H complexes. Fig. 6b presents the temperature-dependent PL spectra for MZNO with

hydrogen. The position of all PL peaks remained unchanged with the temperature change while the quenching occurred at lower temperatures. Based on these PL results, incorporation of oxygen and hydrogen into MZN renders the material opto-electronically active.

Conclusion

MZN thin films were fabricated over a wide composition range by combinatorial sputtering, with a mapping of structural, electronic, and optical properties using spatially-resolved characterization. Material properties of MZNO were altered by modification of cation composition (Mg/(Mg+Zr)) as well as by incorporation of oxygen and hydrogen during growth. Incorporation of hydrogen led to observation of Mg-rich oxide layers at grain boundaries observed by TEM. An interesting trend in the electronic properties was demonstrated: at Mg-rich composition, the carrier concentration was initially higher than 10^{18} cm^{-3}, which was significantly reduced by incorporation of oxygen and hydrogen, down to 10^{14} cm^{-3}. For cation-stoichiometric MZN, the carrier density gradually increased from 10^{19} cm^{-3} to 10^{20} cm^{-3} with increasing oxygen up to 12.5% of O/(N+O). This was decreased down to 10^{19} cm^{-3} if hydrogen was supplied during growth. From this behavior we conclude that donor-like defects such as O_N formed by either excess of O and removed by the presence of hydrogen are critical in controlling the carrier concentration of MZN. Moreover, PL analysis revealed that supplying hydrogen during growth resulted in the enhancement of optoelectronic activity of MZN. Our work shows that tuning the optoelectronic properties of MZN in the presence of hydrogen is possible with controlled addition of oxygen and hydrogen during growth which will help realize the potential of ternary nitrides for device applications.

Conflicts of Interest

There are no conflicts of interest to declare

Acknowledgements

This work was authored at the National Renewable Energy Laboratory, operated by Alliance for Sustainable Energy, LLC, for the U.S. Department of Energy (DOE) under Contract No. DE-AC36-08GO28308. The funding was provided by Office of Science (SC), Office of Basic Energy Sciences (BES), as a part of the Early Career Award "Kinetic Synthesis of Metastable Nitrides" (synthesis, composition, structure and property measurements). This work was also supported by Korea Institute of Energy Technology Evaluation and Planning (KETEP) and the Ministry of Trade, Industry & Energy (MOTIE) of the Republic of Korea (No. 20173010012980), and by Nano-Material Technology Development Program (Green Nano Technology Development Program) through the National Research Foundation of Korea (NRF) funded by the Ministry of Education, Science and Technology (No. 2018M3A7B4065662) (microstructure, SIMS, and photoluminescence measurements). The views expressed in the article do not necessarily represent the views of the DOE or the U.S. Government.

References

1. P. Waltereit, O. Brandt, A. Trampert, H. T. Grahn, J. Menniger, M. Ramsteiner, M. Reiche and K. H. Ploog, *Nature*, 2000, **406**, 865-868.
2. H. Morkoc, *Handbook of Nitride Semiconductors and Devices: Volume 1, Materials Properties, Physics and Growth*, Wiley-VCH Verlag GmbH & Co. KGaA, 2008.
3. S. Q. Wang, I. Raaijmakers, B. J. Burrow, S. Suthar, S. Redkar and K. B. Kim, *J. Appl. Phys.*, 1990, **68**, 5176-5187.

4. B. Shin, Y. Zhu, N. A. Bojarczuk, S. J. Chey and S. Guha, *Appl. Phys. Lett.*, 2012, **101**, 4.

5. K. H. Min, K. C. Chun and K. B. Kim, *J. Vac. Sci. Technol. B*, 1996, **14**, 3263-3269.

6. K. R. Talley, R. Sherbondy, A. Zakutayev and G. L. Brennecka, *Journal of Vacuum Science & Technology A*, 2019, **37**, 060803.

7. S. Kerdsongpanya, N. V. Nong, N. Pryds, A. Žukauskaitė, J. Jensen, J. Birch, J. Lu, L. Hultman, G. Wingqvist and P. Eklund, *Appl. Phys. Lett.*, 2011, **99**, 232113.

8. C. X. Quintela, J. P. Podkaminer, M. N. Luckyanova, T. R. Paudel, E. L. Thies, D. A. Hillsberry, D. A. Tenne, E. Y. Tsymbal, G. Chen, C.-B. Eom and F. Rivadulla, *Advanced Materials*, 2015, **27**, 3032-3037.

9. S. Strite and H. Morkoç, *Journal of Vacuum Science & Technology B: Microelectronics and Nanometer Structures Processing, Measurement, and Phenomena*, 1992, **10**, 1237-1266.

10. T. Shiraishi, Y. Arai and S. Yamazaki, *Journal of Non-Crystalline Solids*, 1985, **77-78**, 1313-1316.

11. R. G. Gordon, D. M. Hoffman and U. Riaz, *Chem. Mat.*, 1992, **4**, 68-71.

12. N. Takahashi, K. Terada and T. Nakamura, *J. Mater. Chem.*, 2000, **10**, 2835-2837.

13. M. N. Solovan, V. V. Brus, E. V. Maistruk and P. D. Maryanchuk, *Inorganic Materials*, 2014, **50**, 40-45.

14. C. M. Caskey, R. M. Richards, D. S. Ginley and A. Zakutayev, *Materials Horizons*, 2014, **1**, 424-430.

15. C. M. Caskey, J. A. Seabold, V. Stevanović, M. Ma, W. A. Smith, D. S. Ginley, N. R. Neale, R. M. Richards, S. Lany and A. Zakutayev, *J. Mater. Chem. C*, 2015, **3**, 1389-1396.

16. A. Zakutayev, C. M. Caskey, A. N. Fioretti, D. S. Ginley, J. Vidal, V. Stevanovic, E. Tea

and S. Lany, *J. Phys. Chem. Lett.*, 2014, **5**, 1117-1125.

17. A. Zakutayev, *J. Mater. Chem. A*, 2016, **4**, 6742-6754.
18. P. Narang, S. Chen, N. C. Coronel, S. Gul, J. Yano, L.-W. Wang, N. S. Lewis and H. A. Atwater, *Advanced Materials*, 2014, **26**, 1235-1241.
19. A. N. Fioretti, A. Zakutayev, H. Moutinho, C. Melamed, J. D. Perkins, A. G. Norman, M. Al-Jassim, E. S. Toberer and A. C. Tamboli, *J. Mater. Chem. C*, 2015, **3**, 11017-11028.
20. A. D. Martinez, A. N. Fioretti, E. S. Toberer and A. C. Tamboli, *J. Mater. Chem. A*, 2017, **5**, 11418-11435.
21. A. N. Fioretti, A. Stokes, M. R. Young, B. Gorman, E. S. Toberer, A. C. Tamboli and A. Zakutayev, *Adv. Electron. Mater.*, 2017, **3**, 5.
22. J. Etourneau, J. Portier and F. Menil, *J. Alloy. Compd.*, 1992, **188**, 1-7.
23. B. Alling, *Phys. Rev. B*, 2014, **89**, 9.
24. Y. Irokawa and M. Usami, *Jpn. J. Appl. Phys.*, 2016, **55**, 3.
25. W. H. Sun, C. J. Bartel, E. Arca, S. R. Bauers, B. Matthews, B. Orvananos, B. R. Chen, M. F. Toney, L. T. Schelhas, W. Tumas, J. Tate, A. Zakutayev, S. Lany, A. M. Holder and G. Ceder, *Nat. Mater.*, 2019, **18**, 732-+.
26. S. R. Bauers, A. Holder, W. H. Sun, C. L. Melamed, R. Woods-Robinson, J. Mangum, J. Perkins, W. Tumas, B. Gorman, A. Tamboli, G. Ceder, S. Lany and A. Zakutayev, *Proc. Natl. Acad. Sci. U. S. A.*, 2019, **116**, 14829-14834.
27. S. R. Bauers, D. M. Hamann, A. Patterson, J. D. Perkins, K. R. Talley and A. Zakutayev, *Jpn. J. Appl. Phys.*, 2019, **58**, 7.
28. B. Wang, S. Kerdsongpanya, M. E. McGahay, E. Milosevic, P. Patsalas and D. Gall, *Journal of Vacuum Science & Technology A*, 2018, **36**, 061501.

29. B. Wang and D. Gall, *Thin Solid Films*, 2019, **688**, 137165.

30. M. H. Du, *J. Mater. Chem. A*, 2014, **2**, 9091-9098.

31. Q. Q. Lin, A. Armin, R. C. R. Nagiri, P. L. Burn and P. Meredith, *Nat. Photonics*, 2015, **9**, 106-112.

32. W. M. Ming, H. L. Shi and M. H. Du, *J. Mater. Chem. A*, 2016, **4**, 13852-13858.

33. A. Miyata, A. Mitioglu, P. Plochocka, O. Portugall, J. T. W. Wang, S. D. Stranks, H. J. Snaith and R. J. Nicholas, *Nat. Phys.*, 2015, **11**, 582-U594.

34. K. Galkowski, A. Mitioglu, A. Miyata, P. Plochocka, O. Portugall, G. E. Eperon, J. T. W. Wang, T. Stergiopoulos, S. D. Stranks, H. J. Snaith and R. J. Nicholas, *Energy Environ. Sci.*, 2016, **9**, 962-970.

35. J. Pan, J. Cordell, C. J. Tucker, A. C. Tamboli, A. Zakutayev and S. Lany, *Advanced Materials*, 2019, **31**, 8.

36. D. C. Hamilton, E. Arca, J. Pan, S. Siol, M. Young, S. Lany and A. Zakutayev, *J. Appl. Phys.*, 2019, **126**, 035701.

37. R. D. Shannon, *Acta Crystallographica Section A*, 1976, **32**, 751-767.

38. M. Futsuhara, K. Yoshioka and O. Takai, *Thin Solid Films*, 1998, **317**, 322-325.

39. J. B. Yoo, H. J. Yoo, H. J. Jung, H. S. Kim, S. Bang, J. Choi, H. Suh, J. H. Lee, J. G. Kim and N. H. Hur, *J. Mater. Chem. A*, 2016, **4**, 869-876.

40. T. L. Brown, *Chemical Thermodynamics of Zirconium*, Elsevier, 2005.

41. J. Rumble, *CRC Handbook of Chemistry and Physics, 100th Edition*, CRC Press, 2019.

42. V. Stevanović, S. Lany, X. Zhang and A. Zunger, *Phys. Rev. B*, 2012, **85**, 115104.

43. N. Preissler, O. Bierwagen, A. T. Ramu and J. S. Speck, *Phys. Rev. B*, 2013, **88**, 085305.

44. L. Gupta, A. Mansingh and P. K. Srivastava, *Thin Solid Films*, 1989, **176**, 33-44.

45. Z. Chen, L. Huang, Q. Zhang, Y. Xi, R. Li, W. Li, G. Xu and H. Cheng, *The Journal of Physical Chemistry C*, 2015, **119**, 4789-4795.

46. J. Wu, W. Walukiewicz, S. X. Li, R. Armitage, J. C. Ho, E. R. Weber, E. E. Haller, H. Lu, W. J. Schaff, A. Barcz and R. Jakiela, *Appl. Phys. Lett.*, 2004, **84**, 2805-2807.

47. J. Neugebauer and C. G. Van De Walle, *Phys. Rev. Lett.*, 1995, **75**, 4452-4455.

48. J. Neugebauer and C. G. Van de Walle, *Appl. Phys. Lett.*, 1996, **68**, 1829-1831.

49. S. R. Bauers, J. Mangum, S. P. Harvey, J. D. Perkins, B. Gorman and A. Zakutayev, *Appl. Phys. Lett.*, 2020, **116**, 102102.